J. Fluid Mech. (2025), *vol.* 1016, A23, doi:10.1017/jfm.2025.10428

JFM PAPERS

A model spectrum for turbulent wall-bounded flow

Nikolay Gustenyov,[1] Sean C.C. Bailey[1] and Alexander J. Smits[2]

[1]Dept. of Mechanical and Aerospace Engineering, University of Kentucky, Lexington, KY 40506, USA
[2]Dept. of Mechanical and Aerospace Engineering, Princeton University, Princeton, NJ 08544, USA
Corresponding author: Alexander J. Smits, asmits@princeton.edu

(Received 6 February 2025; revised 2 June 2025; accepted 25 June 2025)

A model is proposed for the one-dimensional spectrum and streamwise Reynolds stress in pipe flow for arbitrarily large Reynolds numbers. Constructed in wavenumber space, the model comprises four principal contributions to the spectrum: streaks, large-scale motions, very-large-scale motions and incoherent turbulence. It accounts for the broad and overlapping spectral content of these contributions from different eddy types. The model reproduces well the broad structure of the premultiplied one-dimensional spectrum of the streamwise velocity, although the bimodal shape that has been observed at certain wall-normal locations, and the $-5/3$ slope of the inertial subrange, are not captured effectively because of the simplifications made within the model. Regardless, the Reynolds stress distribution is well reproduced, even within the near-wall region, including key features of wall-bounded flows such as the Reynolds number dependence of the inner peak, the formation of a logarithmic region, and the formation of an outer peak. These findings suggest that many of these features arise from the overlap of energy content produced by both inner- and outer-scaled eddy structures combined with the viscous-scaled influence of the wall. The model is also used to compare with canonical turbulent boundary layer and channel flows, and despite some differences being apparent, we speculate that with only minor modifications to its coefficients, the model can be adapted to these flows as well.

Key words: boundary layer structure, turbulence modelling, turbulent boundary layers

1. Introduction

A model is proposed for the one-dimensional streamwise spectrum (and its integral, the streamwise Reynolds stress) that applies to turbulent pipe flow for arbitrarily large Reynolds numbers. The model incorporates the contributions made by the organised motions found in wall-bounded turbulence (see Smits *et al.* 2011*a*), specifically, the near-wall streaks, the large-scale motions (LSM), which take in the hairpin vortices as part of their structure, and very-large-scale motions (VLSM or superstructures), as well as the incoherent (i.e. homogeneous) contributions.

This effort draws most closely on the model originally advanced by Perry (1982) and Perry, Henbest & Chong (1986), that was in turn based on the Townsend (1976) attached-eddy hypothesis. This model, and its subsequent developments into the attached-eddy model (Marusic & Monty 2019), provides a kinematic description for wall-bounded turbulence that incorporates the 'attached' eddies (those that scale with the distance to the wall, y), together with some form of large outer-scale 'detached' eddies (that scale with the boundary layer thickness δ), and proposes that the statistical features of wall-bounded turbulence can be modelled by a linear superposition of such eddies. The model is inviscid, in that it applies only for $y^+ > 100$ (the lowest level of the attached-eddy hierarchies). Here, $y^+ = yu_\tau/\nu$, where $u_\tau = (\tau_w/\rho)^{1/2}$ is the friction velocity, τ_w is the shear stress at the wall, and ρ and ν are the fluid density and the kinematic viscosity, respectively.

In addition, Perry *et al.* (1986) advanced scaling arguments based on the contributions of these structures to the one-dimensional streamwise spectrum in the inertial region (approximately corresponding to $100\nu/u_\tau < y < 0.12\delta$). It was proposed that at sufficiently high Reynolds number, there might exist an overlap region in wavenumber space between the (inner) attached eddies, scaling on y, and the (outer) detached eddies, scaling on δ, where δ in general is the outer length scale (the boundary layer thickness, pipe radius or channel half-height). This leads to the presence of a k_1^{-1} region in the spectrum, where k_1 is the component of the wavenumber vector aligned with the streamwise direction. Similarly, it was proposed that there could be an overlap region between the attached eddies and the (isotropic) viscous-scaled motions, which leads to the presence of a $k_1^{-5/3}$ region, in agreement with Kolmogorov's hypothesis. The region where we might expect k_1^{-1} scaling corresponds to the wavenumbers occupied by the LSM, but experiments have since shown that although the LSM appear to behave as attached motions, they do not scale simply as k_1^{-1} (Vallikivi, Ganapathisubramani & Smits 2015). Also, we now have a better understanding of the structure of the outer-layer motions, especially the importance of the VLSM, where at high Reynolds numbers, the low-wavenumber VLSM contribute approximately half of the total energy content of the streamwise turbulence component (Smits *et al.* 2011*a*).

To develop a new spectral model that specifically incorporates our current understanding of these organised motions, and that will apply not just to the inertial region at high Reynolds number but across the entire boundary layer at all Reynolds numbers, we will represent the contribution to energy content made by the near-wall viscous motions, the LSM and the VLSM using log-normal distributions in the streamwise wavenumber, as first suggested by Smits (2010) and supported by the measurements of Rosenberg *et al.* (2013) and Vallikivi *et al.* (2015) in pipe and boundary layer flows. These distributions thus model the contribution to streamwise energy content by each type of organised motion in the form of statistical distributions in wavenumber space. To model the wall dependence of the contributions from homogeneous turbulence, we utilise the recent work of Gustenyov *et al.* (2023), who found that small-scale turbulent structure, when characterised by the Kolmogorov length scale, follows inner scaling throughout the entire boundary layer thickness, while energetic structures characterised by a statistically based large scale follow outer scaling over the same extent. In addition, the integrated one-dimensional energy spectrum gives the streamwise Reynolds normal stress $\overline{u_1^2}$, so the model also gives the wall-normal distribution of $\overline{u_1^2}$ over an arbitrarily wide range of Reynolds numbers, in good agreement with the available data, as will be shown. Similar models have also been produced for Reynolds number and wall-distance dependence of $\overline{u_1^2}$ (e.g. Marusic & Kunkel 2003); however, the present model provides new insight into the streamwise energy content that produces these dependencies.

We will assume that these four separate contributions to the one-dimensional energy spectrum add linearly, thereby neglecting any modulation or other nonlinear interactions. In fact, it can be shown that the nonlinear interactions are weak, thus make little contribution to the turbulence energy. For example, in the model proposed by Marusic, Mathis & Hutchins (2010), the near-wall turbulence u_p^+ is represented by a 'universal' signal u^* that experiences both a superimposition (characterised by a coefficient α) and a nonlinear modulation (characterised by a coefficient β) by the large-scale outer-layer motion u_{OL}^+, typically taken from a point within the log region. That is, instantaneously,

$$u_p^+(y^+) = u^*(y^+)\left[1+\beta(y^+)\, u_{OL}^+\right] + \alpha(y^+)\, u_{OL}^+. \tag{1.1}$$

Since u^* and u_{OL}^+ are uncorrelated by definition, the averages of odd moments are zero, and by taking the mean square, we obtain

$$\overline{u_p^{+2}} = \overline{u^{*2}} + \beta^2\, \overline{\left(u^*\, u_{OL}^+\right)^2} + \alpha^2\, \overline{u_{OL}^{+\,2}}. \tag{1.2}$$

For the case cited by Mathis, Hutchins & Marusic (2011), at $y^+ = 15$ and $Re_\tau = 7000$, we find that the nonlinear contribution, represented by the second term in (1.2), amounts to less than 1 % of the total energy. In Appendix A we show that this is a general result. Thus a linear summation of eddy contributions appears to be a reasonable starting basis for our model.

In the following, we first present the broad framework of the model using some illustrative examples, before delving into its details. We then demonstrate the model's ability to reproduce the spectrum and streamwise Reynolds stress distributions for pipe flows by comparing its output to available direct numerical simulations (DNS) and experimental data spanning a range $Re_\tau \approx 180$ to 1 00 000. Although the model does not capture all details of the spectrum, as previously noted, it indicates where energy is stored and accurately reproduces the Reynolds number dependence of the integrated energy in the form of wall-normal profiles of streamwise Reynolds stress. Furthermore, even though the model was developed for pipe flow, the conceptual approach is applicable to other canonical flows. Thus we also assess the model against turbulent boundary layer and channel flows, and demonstrate that our approach also applies well to these flows.

2. Model approach

2.1. *Basic model formulation*

We construct the model for the longitudinal one-dimensional velocity spectrum E_{11} in the streamwise, x-aligned, wavenumber domain k_1, using functions that depend on both k_1 and y, the distance from the wall. The model has contributions from four eddy populations, broadly representing the coherent LSM (f_1), VLSM (f_2) and near-wall streaks (f_3), as well as the incoherent homogeneous isotropic turbulence (HIT) arising from the breakdown of these organised motions as they transport away from the wall (f_{HIT}). These distributions are modelled as premultiplied forms of E_{11} (i.e. $k_1 E_{11}$) that overlap in wavenumber space (reflecting the broad range of spectral content in each class of coherent motions), and the energy contained at each wavenumber is taken to be a linear summation over all eddy types. That is, we propose

$$k_1 E_{11}/u_\tau^2 = f_1 + f_2 + f_3 + f_{HIT}, \tag{2.1}$$

where $\overline{u_1^2}$ can then be obtained by integrating E_{11} over all k_1. The additive structure of (2.1) was selected because the energy content attributed to different modes of motion appeared to be simply superimposed in the premultiplied energy spectrum. A similar decomposition of the premultiplied energy content into different eddy structures was proposed schematically for turbulent boundary layers by Hutchins & Marusic (2007).

For the coherent motions (f_1, f_2 and f_3), we will assume that their premultiplied energy distribution can be approximated using a log-normal distribution in wavenumber. This formulation is motivated by observations of multiple peaks in the premultiplied spectrum (which, in turn, motivated the decomposition of long-wavelength streamwise energy content into separate contributions that were identified as LSM and VLSM or superstructures, and observations that this bimodal structure can be reproduced by a superposition of two log-normal distributions (Kim & Adrian 1999; Smits 2010). Note that existing model spectra representing HIT at high Reynolds number, e.g. the model presented by Pope (2000), also take on a nearly log-normal form when presented in premultiplied one-dimensional form. We thus treat each of f_1, f_2 and f_3 as an individual eddy population as with a broad distribution of associated energy produced at a characteristic wavenumber, and use the Pope (2000) model for f_{HIT}.

Hence we propose that

$$f_n = A_n \exp\left[-\left(\frac{\log_{10}(k_1 y) - \log_{10}(\mu_n)}{\log_{10}(\sigma_n)}\right)^2\right], \tag{2.2}$$

where $n = 1, 2, 3$ indicate the distributions corresponding to high-wavenumber (LSM), lower-wavenumber (VLSM) and near-wall (streaks) energy distributions, respectively. The energy content is thus distributed around the (non-dimensional) wavenumbers at which each eddy type is produced, μ_n, with the wavenumber range of the distribution described by σ_n, and the amplitude by A_n. The three terms A_n, μ_n and σ_n depend on y and introduce the wall-dependent scaling of f_1, f_2 and f_3, with their precise formulation described in the following subsections.

Two points need to be made. First, (2.2) is implicitly unable to reproduce the predicted k^{-1} scaling region predicted by the attached-eddy hypothesis. However, as noted by Vallikivi *et al.* (2015), the existing data have not revealed an extended region of k^{-1} scaling even at very high Reynolds numbers, and as will be presented later, the log-normal distributions used here are able to reproduce many key features of the streamwise energy content without imposing this constraint. This is particularly relevant for the present model, because it covers even the lowest Reynolds numbers, where k^{-1} scaling is not expected to hold under any circumstances. Second, we cannot expect an accurate reproduction of the high-wavenumber universal equilibrium range, therefore this model is currently limited to reproducing the energy-containing range of the streamwise velocity fluctuations. That said, for the 'incoherent motions', we will use

$$f_{HIT} = \left(k_1 E_{11}^{HIT}/u_\tau^2\right)(y/\delta)^n\,, \tag{2.3}$$

where E_{11}^{HIT} is found from transformation of the three-dimensional spectrum model of Pope (2000) to a one-dimensional form. The function f_{HIT} is intended to account for incoherent motions that form as a result of the natural breakdown of coherent motions.

	Case 1	Case 2	Case 3	Case 4	Case 5	Case 6	Case 7	Case 8
Symbol	●	●	●	★	★	★	▲	▲
$Re_\tau = \delta u_\tau/\nu$	2000	3300	5400	10 500	20 400	38 200	70 000	1 00 000
$\ell^+ = \ell u_\tau/\nu$	1.8	3.1	5.0	9.7	19	35	65	93

Table 1. Superpipe flow experimental conditions; from Hultmark *et al.* (2012, 2013).

This energy content will have an increased prominence farther away from the wall, and the $(y/\delta)^n$ dependence with $n = 1.1$ was found to capture this dependence for pipe flows.

2.2. *Development and validation datasets*

To develop and validate the model, we use experimental data covering $180 \leq Re_\tau \leq 1\,00\,000$ (see table 1). We mainly use the Superpipe data acquired at Princeton University (Hultmark *et al.* 2012, 2013; Vallikivi *et al.* 2015), encompassing a Reynolds number range $2000 \leq Re_\tau \leq 100\,000$. NSTAP probes (Vallikivi & Smits 2014) were used for these experiments, with non-dimensional sensor lengths $\ell^+ = \ell u_\tau/\nu$ as given in the table. Where appropriate, the spatial filtering correction of Smits, McKeon & Marusic (2011*a*) was applied, and Taylor's hypothesis (Taylor 1938) was used to transform the time-dependent measurement to the spatial domain, so that $k_1 \approx 2\pi f/\overline{U_1}$, where f is the frequency, and $\overline{U_1}$ is the mean velocity. Because Taylor's hypothesis can potentially introduce abnormalities in the spectrum (e.g. Moin 2009), for additional validation we use DNS data in the range $180 \leq Re_\tau \leq 6000$ (Pirozzoli *et al.* 2021), and the Reynolds stress profiles obtained from particle image velocimetry (PIV) measurements in the CICLoPE facility in the range $5400 \leq Re_\tau \leq 40\,000$ (Willert *et al.* 2017). Additional statistical information from CICLoPE measurements provided by Fiorini (2017) and from DNS described by Ahn *et al.* (2013, 2015), Wu & Moin (2008), El Khoury *et al.* (2013), Chin, Monty & Ooi (2014) and Yao *et al.* (2023) is also used.

2.3. *Overview*

Before describing the model in detail, we give an example to illustrate how each of the functions f_n contributes to the premultiplied wavenumber spectrum, and how the model spectrum compares to that measured in a high-Reynolds-number pipe flow experiment. Figure 1 shows the measured premultiplied spectrum for six y-locations at $Re_\tau = 10\,500$. As already noted, the appearance of double peaks in the spectrum has been linked previously to the contributions made by the LSM and VLSM by Kim & Adrian (1999) and Vallikivi *et al.* (2015), among others. This characteristic structure was observed at all Reynolds numbers considered, over a relatively wide range of wall-normal distances. The figure also shows the corresponding model spectra, and the contributions made by each of the four eddy functions f_1 to f_{HIT}. Although the model does not reproduce this bimodal feature of the premultiplied spectra, it captures well the broad energy content over the entire range of wall-normal distances shown. It may be possible to reproduce the spectra more accurately by using other representations for the eddy populations instead of the relatively simple log-normal populations used here, but this would require additional complexity that we sought to avoid. In addition, we note that for the spectrum nearest the wall, at $y^+ = 16$, the model appears to over-predict the energy content. However, at this location $y/\ell = O(1)$, and some degree of spatial filtering of the experimental energy

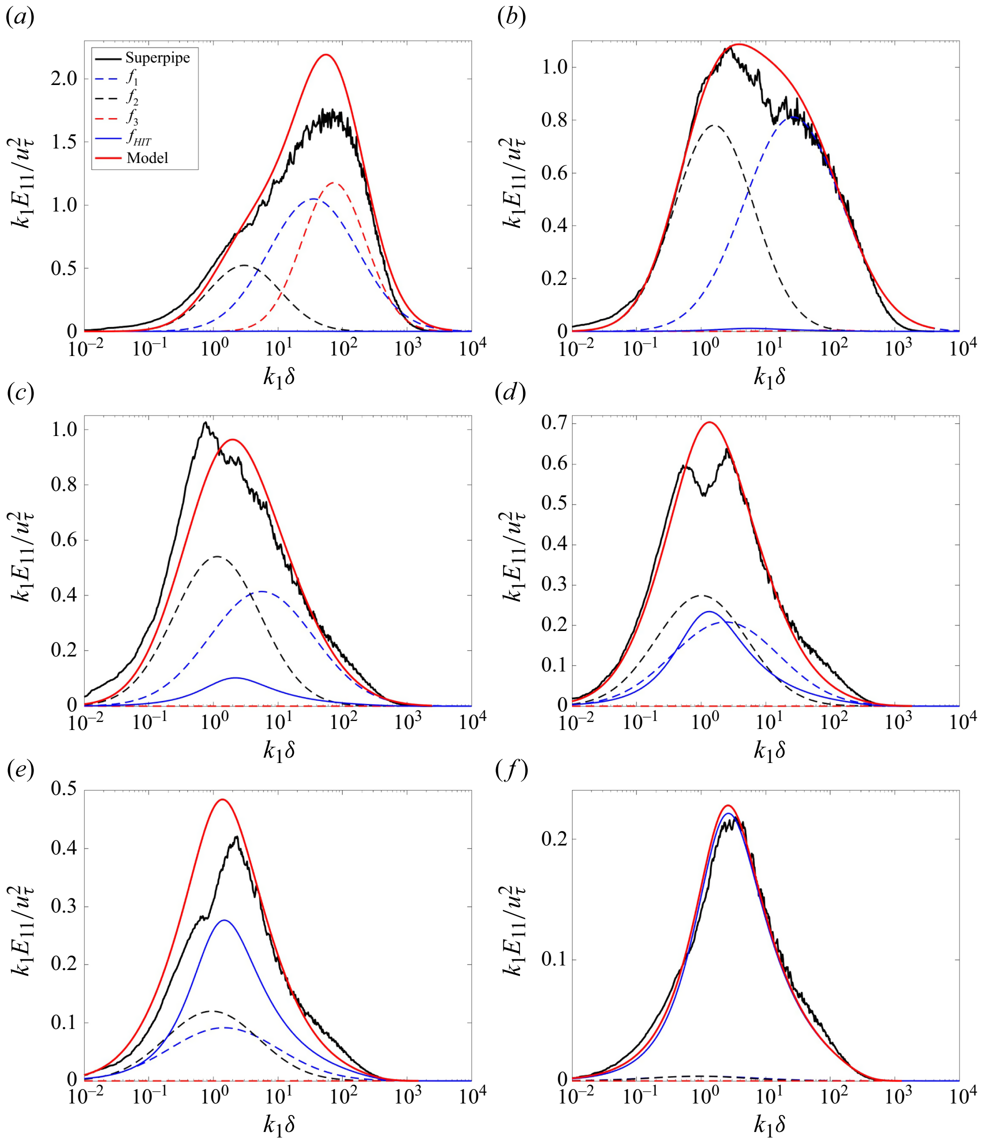

Figure 1. Premultiplied energy spectra for pipe flow at $Re_\tau = 10\,500$: (*a*) $y/\delta = 0.001536$ ($y^+ = 16$), (*b*) $y/\delta = 0.011$ ($y^+ = 116$), (*c*) $y/\delta = 0.1$ ($y^+ = 1053$), (*d*) $y/\delta = 0.314$ ($y^+ = 3303$), (*e*) $y/\delta = 0.6$ ($y^+ = 6328$), (*f*) $y/\delta = 0.979$ ($y^+ = 10\,299$).

content is to be anticipated (Smits 2022). In terms of the separate contributions to the streamwise energy, f_1 and f_2 are important at almost all wall-normal locations, f_3 is significant only near the wall, and f_{HIT} has its greatest contribution in the outer region of the flow.

A comparison of the measured and model spectra at the same wall-normal locations in log-log form is presented in figure 2(*a*). This presentation highlights the differences between the measured and model spectra at low wavenumber, where there is little energy content, and at high wavenumber, where the log-normal basis functions used to construct the model are unable to reproduce the highest wavenumber content within the universal

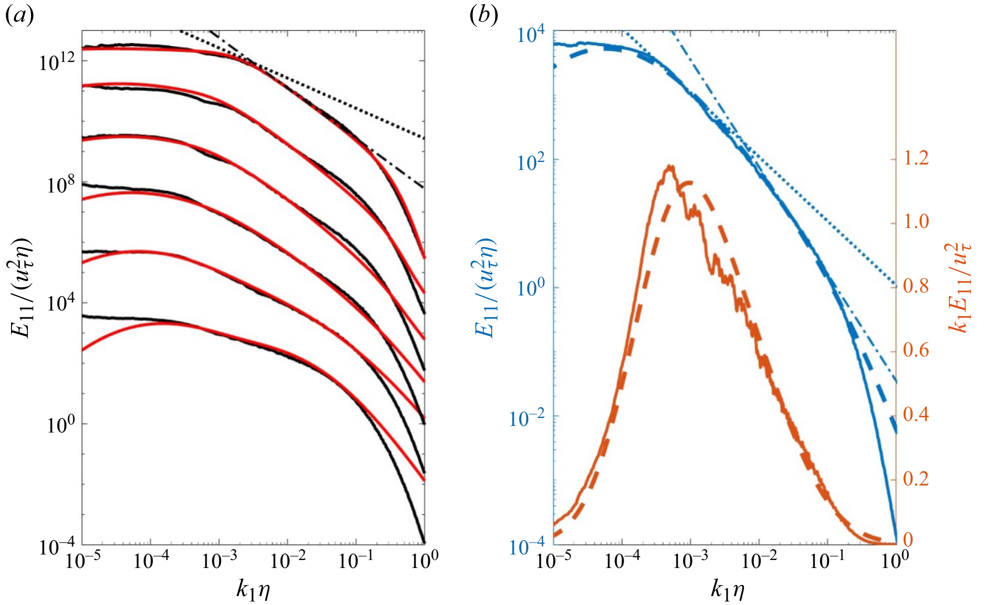

Figure 2. Energy spectra for pipe flow at $Re_\tau = 10\,500$. (*a*) Same y locations as shown in figure 1, with the spectrum for $y^+ = 16$ on the bottom, and increasing y locations shown successively shifted by two orders of magnitude. Solid black lines indicate measurement, and red lines indicate model prediction. (*b*) Energy spectrum at $y/\delta = 0.037$ ($y^+ = 390$) shown in both log-log and premultiplied form. The solid line indicates the measurement, and the dashed line indicates the model prediction. In both (*a*) and (*b*), the dash-dotted line indicates the $k_1^{-5/3}$ slope, and the dotted line indicates the k_1^{-1} slope.

equilibrium range. That said, the superposition of eddy populations appears to reproduce the $k_1^{-5/3}$ slope of the inertial subrange in the outer layer. This is further illustrated in figure 2(*b*), which presents the measured and modelled spectrum at $y^+ = 390$, or $y/\delta = 0.037$ – a location within the expected range of the overlap layer (Marusic *et al.* 2013). Here, the attached-eddy hypothesis predicts that an overlap of y-scaled and δ-scaled eddies will produce a k_1^{-1} spectral roll-off (e.g. Perry & Abell 1977). Figure 2(*b*) shows that such a region appears to be present, at least approximately, in both the measured and modelled spectra at this location. However, a k_1^{-1} region would appear as a plateau in the premultiplied form of the spectra, and as noted by Vallikivi *et al.* (2015) among others, there is little evidence of such a plateau in the premultiplied form of the measured spectrum (as also shown in figure 1).

2.4. *The LSM and VLSM (f_1 and f_2)*

We now consider the detailed formulation of f_1 (LSM) and f_2 (VLSM), i.e. how the specific functions $\mu_{1,2}$, $A_{1,2}$ and $\sigma_{1,2}$ were established as a function of wavenumber, wall distance and Reynolds number. The general approach was to use anticipated scaling behaviour whenever known, but allowing for alternative forms when they better approximated the available empirical evidence. The final forms of these coefficients are compromises that best describe the energy content contributed by each of the modelled motions while maintaining as much as possible prior theoretical and empirical considerations.

As a starting point, we seek expressions to describe the y dependence of μ_1 and μ_2. To do so, we find the wavenumbers corresponding to the LSM and VLSM peaks in the

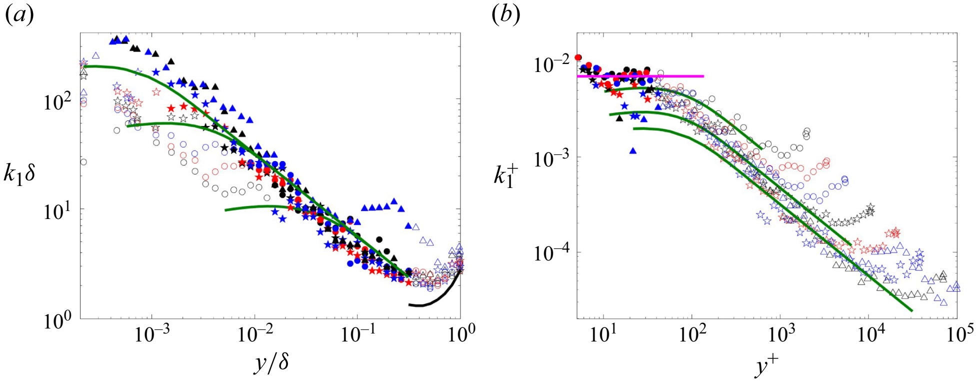

Figure 3. Wall-normal dependence of the peak associated with LSM in (*a*) outer scaling and (*b*) inner scaling. The green lines in (*a*) indicate $\mu_1\delta/y$ for $Re_\tau = 2000$, 20 400 and 1 00 000, and the black line shows the peak of f_{HIT} (see (2.3)). In (*b*), the green lines show μ_1/y^+ for $Re_\tau = 2000$, 20 400 and 1 00 000, and the pink line marks μ_3/y^+ (see (2.12)). The symbols and colours are given in table 1, with the filled symbols used to indicate when $y^+ > 30$ and $y/\delta \leq 0.3$ in (*a*), and when $y^+ \leq 30$ in (*b*).

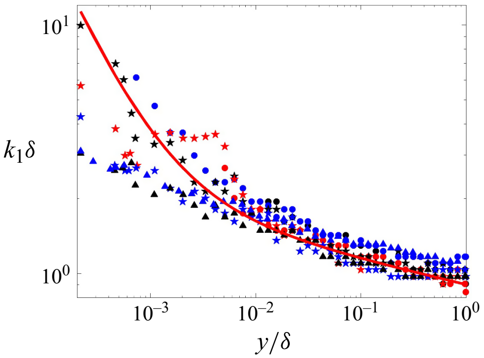

Figure 4. Wall-normal dependence of the peak associated with VLSM in outer scaling. The red line marks $\mu_2\delta/y$, where μ_2 is given by (2.4). The symbols and colours are given in table 1.

experimental spectra by smoothing the premultiplied spectra using a moving average, and then fitting two log-normal distributions to the data, following the approach used by Rosenberg *et al.* (2013) and Vallikivi *et al.* (2015). The results are shown in figures 3 and 4, respectively, and they are similar in all respects to the results obtained earlier by Vallikivi *et al.* (2015).

For the VLSM peak (figure 4), the wall-normal dependence of the peak location was then modelled using outer scaling as

$$\mu_2 = 0.002 + 0.9(y/\delta)^{0.9}. \tag{2.4}$$

This formulation follows the power-law dependence observed by Vallikivi *et al.* (2015), although with slightly different coefficients – a consequence of the scatter in the observed spectral peak near the wall. However, the contribution of the f_2 eddy population to the energy spectrum in this region is relatively small, and (2.4) was found to provide a reasonable representation of the VLSM peak variation with wall distance.

The behaviour of the LSM peak is more complex, as shown in figure 3. For $y^+ > 30$ and $y/\delta \leq 0.3$, it follows outer scaling and is well represented by $y/\delta^{0.25}$ (figure 3*a*), but near the wall, the peak is better represented by inner scaling, as also observed by

Vallikivi *et al.* (2015). Hence we propose

$$\mu_1 = \left[1 - (\exp[-y^+])^{0.02}\right](y/\delta)^{0.25}, \tag{2.5}$$

where the inner-scaled term is introduced to shift μ_1 to lower wavenumbers when $y^+ \lessapprox 200$, to approximate the increased dependence on inner scaling near the wall. Even with this modification, as illustrated in figure 3(*b*), there are still significant differences between (2.5) and the experimentally observed peak wavenumber for $y^+ < 100$. Nevertheless, when f_1 was combined with f_3, the LSM peak location in this range was found to be well approximated by (2.5), as will be shown later. In addition, we see that for $y/\delta > 0.3$, the location of the f_1 peak deviates from (2.5). However, at these wall-normal distances, the LSM and VLSM peaks are more difficult to distinguish (Vallikivi *et al.* 2015), and we can anticipate a large contribution to energy from incoherent eddies, which are represented here by f_{HIT}.

With $\mu_{1,2}$ established, $A_{1,2}$ and $\sigma_{1,2}$ can be determined. For the amplitude of A_1 (LSM), since f_1 represents the structures most closely related to the attached structures of Perry (1982), we can anticipate a logarithmic contribution to the Reynolds stress in outer scaling. Hence we propose that

$$A_1 = -0.18 m_v \ln(y/\delta), \tag{2.6}$$

where

$$m_v = (1 - \exp[-0.25 y^+])^6 \tag{2.7}$$

and m_v is introduced to reflect the viscous damping introduced by the wall. The expression for m_v was chosen to match the near-wall decay in energy content and is not based on any established theoretical model.

In addition, since the VLSM are connected to the LSM eddies, as suggested by Adrian (2007), Monty *et al.* (2007) and others, we can expect that the wall-normal dependence of the VLSM would also take a logarithmic form. However, f_2 provides the largest contribution to the streamwise energy content from wavelengths larger than δ, and therefore to the outer-layer signal u_{OL}^+ in (1.1). Following (1.2), and neglecting the nonlinear interactions, we can therefore anticipate the near-wall contribution by the VLSM to provide a good approximation for the level of outer-layer influence described by (1.2). Using this guidance, we propose that

$$A_2 = -0.24\, m_v\, \alpha^2 \ln\left[(y/\delta) + 0.005\right], \tag{2.8}$$

where

$$\alpha = 1 - 0.36 \exp[-0.01 y^+]. \tag{2.9}$$

The formulation of α was determined through a fit applied to the values measured by Mathis *et al.* (2011), and the leading-order outer-scale dependence is damped by m_v in the identical way used for A_1. Although Mathis *et al.* (2011) determined $\alpha(y^+)$ from measurements taken in turbulent boundary layer measurements (see also Mathis *et al.* 2009*b*), we expect the near-wall behaviour to be similar for all canonical geometries, therefore we also apply it unchanged to pipe flows.

Finally, we consider the widths of these eddy populations, σ_n. We have little guidance here, aside from the expectation that they follow outer scaling (Vallikivi *et al.* 2015), therefore these values were determined empirically in a manner that best reconstructed the measured spectra. This procedure gave

$$\sigma_1 = 16 + \ln\,(y/\delta) \tag{2.10}$$

and

$$\sigma_2 = 1 + 10(y/\delta)^{0.1}. \tag{2.11}$$

Taken together, we expect f_1 and f_2 to largely dictate the streamwise Reynolds stress distributions for $y^+ > 30$ and $y/\delta < 0.7$, and result in the formation of a logarithmic region in the turbulence within this range (as will be presented in § 3.2).

2.5. *Near-wall streaks (f_3)*

For $y^+ < 30$, the near-wall production mechanism becomes the main contributor to the overall velocity variance. Hence we expect f_3 to become increasingly important in this range, and that it will scale on inner variables. Furthermore, this function can also be considered to represent the universal signal u^* in (1.1). Following the procedure used for f_1 and f_2, we identify μ_3 using the location of the near-wall peak in the measured spectra. As illustrated in figure 3(*b*), for $y^+ > 8$, the near-wall peak occurs at $k_1^+ = 0.007$, closely corresponding to the $\sim 1000\nu/u_\tau$ wavelength attributed to the near-wall streaks (Kline *et al.* 1967). Therefore, we let

$$\mu_3 = 0.007 y^+. \tag{2.12}$$

To describe the wall-normal and wavenumber dependence of the inner spectral peak, we use

$$A_3 = 1.6 \exp\left[-\left(0.945 \ln\left(0.11 y^+\right)\right)^2\right] \tag{2.13}$$

and

$$\sigma_3 = 5, \tag{2.14}$$

as determined by examining measured spectra that approximate the form of a joint log-normal distribution of energy in both inner-scaled wavenumber and wall-distance.

2.6. *Incoherent motions (f_{HIT})*

We anticipate that the coherent eddies represented by f_1, f_2 and f_3 co-exist with disorganised (i.e. incoherent) turbulence that develops due to the breakdown of the coherent eddies and is transported away from the wall via turbulent advection. We model this contribution to the one-dimensional spectrum as being approximately homogeneous and isotropic, even though these eddies are expected to be anisotropic at low wavenumber. We begin with the Pope (2000) three-dimensional spectrum, where

$$E^{HIT}(k) = C\bar{\varepsilon}^{2/3} k^{-5/3} f_L f_\eta. \tag{2.15}$$

Here, $\bar{\varepsilon}$ is the mean dissipation rate, k is the magnitude of the three-dimensional wavenumber vector, and C is the Kolmogorov constant. The primary feature of this model is the inertial subrange distinguished by the $k^{-5/3}$ scaling. The function f_L describes the energy-containing range using L as a length scale characterising large eddies such that

$$f_L = \left(\frac{kL}{[(kL)^2 + C_L]^{1/2}}\right)^{5/3+p_0}, \tag{2.16}$$

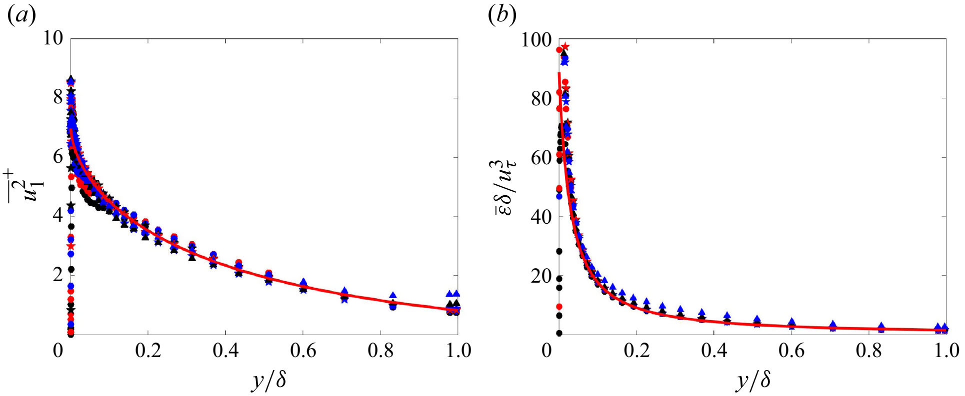

Figure 5. (*a*) Inner-scaled streamwise velocity variance with (2.20) shown using a solid red line. (*b*) Normalised mean dissipation rate $\overline{\varepsilon}$ with (2.21) shown using a red line. Symbols and colours are consistent with table 1.

where C_L is a positive constant and $p_0 = 4$. At small wavenumbers, (2.16) approximates the von Kármán (1948) interpolation equation with $E(k) \sim k^4$, whereas at large k, (2.16) approaches unity such that (2.15) transitions to the inertial subrange. The function f_η describes the small-scale dissipation range, and scales with the Kolmogorov length scale $\eta = (\nu^3/\overline{\varepsilon})^{1/4}$. Specifically, f_η is defined as

$$f_\eta = \exp\left(-\gamma\left(\left[(k\eta)^4 + C_\eta^4\right]^{1/4} - C_\eta\right)\right), \tag{2.17}$$

and tends to unity at small k, and zero at large k. In (2.17), both γ and C_η are positive constants. For a specified L and η, the three-dimensional model spectrum can be determined using (2.15), (2.16) and (2.17) with $C = 1.5$ and $\gamma = 5.2$ (Saddoughi & Veeravalli 1994), while constants C_L and C_η are dictated by the requirement that $E^{HIT}(k)$ and $2\nu k^2\, E^{HIT}(k)$ integrate to the turbulent kinetic energy and $\overline{\varepsilon}$, respectively, at the centreline. Here, the best agreement with the measured values was found when $C_L = 3.2$ and $C_\eta = 0.41$. The eddy population representing these motions is thus found from (2.15), (2.16) and (2.17) using y-dependent values for L, and η. The result is then transformed to a one-dimensional spectrum using

$$E_{11}^{HIT}(k_1) = \int_{k_1}^{\infty} \frac{E^{HIT}(k)}{k}\left(1 - \frac{k_1^2}{k^2}\right)\mathrm{d}k, \tag{2.18}$$

and then added to (2.1) using (2.3).

We therefore need wall-normal-dependent expressions for L and $\overline{\varepsilon}$. We focus on the outer layer because we expect f_{HIT} to have the most influence in that region due to the breakdown of near-wall coherent eddies and subsequent transport of the resulting incoherent turbulence away from the wall.

For the y dependence of L, we use

$$L \approx \left(\tfrac{3}{2}\overline{u_1^2}^+\right)^{3/2} u_\tau^3/\overline{\varepsilon}. \tag{2.19}$$

Bailey & Witte (2016) demonstrated that this length scale is a better choice than the integral scale in describing the low-wavenumber bound of the inertial subrange as the Reynolds number and wall-normal distance vary. The wall dependence of $\overline{\varepsilon}$ was estimated from the measured time series using one-dimensional approximations (Gustenyov *et al.* 2023). As illustrated in figures 5(*a*) and 5(*b*), $\overline{u_1^2}^+$ and $\overline{\varepsilon}$ scale with outer variables over the full extent of the outer layer (where f_{HIT} becomes increasingly important) over the entire Reynolds number range available. We see that

$$\overline{u_1^2}^+ \approx 0.15\big(2.5 - (y/\delta)^{0.6}\big)^{4.2} \tag{2.20}$$

and

$$\frac{\overline{\varepsilon}\delta}{u_\tau^3} \approx 1.6\,(y/\delta + 0.035)^{-1.2} \tag{2.21}$$

provide reasonable approximations for the wall dependence of $\overline{u_1^2}^+$ and $\overline{\varepsilon}$, although other expressions are likely to be as effective. Equations (2.19)–(2.21) can then be used to determine L and η, and hence f_{HIT} from (2.3).

3. Comparing model results with pipe flow data

In comparing the results of the model with pipe flow data, we look for some specific features. These include: (i) the formation of a logarithmic scaling region in the Reynolds stress distribution consistent with the attached-eddy hypothesis; (ii) the Reynolds number dependence of the near-wall peak in the Reynolds stress distribution that indicates that the near-wall energy content does not follow inner scaling; (iii) the formation of an outer peak in the Reynolds stress distribution at high Reynolds numbers; and (iv) the formation of an outer peak in the spectral maps. We will start by considering the results at $Re_\tau = 10\,500$, shown preliminarily in figure 1, in more detail, using contour maps of the premultiplied spectra and the wall normal distributions of the streamwise turbulence stress. We then examine the Reynolds number dependence of the stress distributions before returning to the spectral maps.

3.1. *Comparisons at* $Re_\tau = 10\,500$

The contour maps of the premultiplied spectra are given in figure 6. Figure 6(*a*) shows how the energy content provided by f_1, f_2 and f_3 in the inner layer transitions to being mostly provided by f_1 and f_2 in the overlap layer, and how f_{HIT} plays an increasingly important role as y/δ approaches unity. Figure 6(*b*) shows the total distribution found by summing all four terms, and figure 6(*c*) displays the corresponding contour map obtained by experiment. Overall, the model appears to capture the energy distribution of the measured spectra well at this Reynolds number. Most notably, the inner peak centred on $k_1\delta = 75,\ \ y^+ = 15$ is represented accurately. Also reproduced well is the outer peak in the spectral map, appearing near $k_1\delta = 2.8,\ \ y/\delta \approx 0.05$, although the details are not as sharp as those observed in the experiment. As previously mentioned, this is a consequence of the log-normal form of the eddy population, which, although simple to implement from a modelling perspective, is less likely to capture some of the details of the spectral distributions. In particular, as noted earlier in the discussion of figure 1, the model is not able to reproduce the bimodality of the spectral content evident in figure 6(*c*) for $y/\delta > 0.1$.

By integrating the energy spectra, we obtain the wall-normal distributions of $\overline{u_1^2}^+$, and the individual contributions made by the four eddy functions. The model output is compared to the corresponding Superpipe profile in figure 6(*d*), and we see very good agreement for the overall energy content. The near-wall peak is seen to be formed by the superposition of f_1, f_2 and f_3, and, consistent with the concept of detached eddies, the

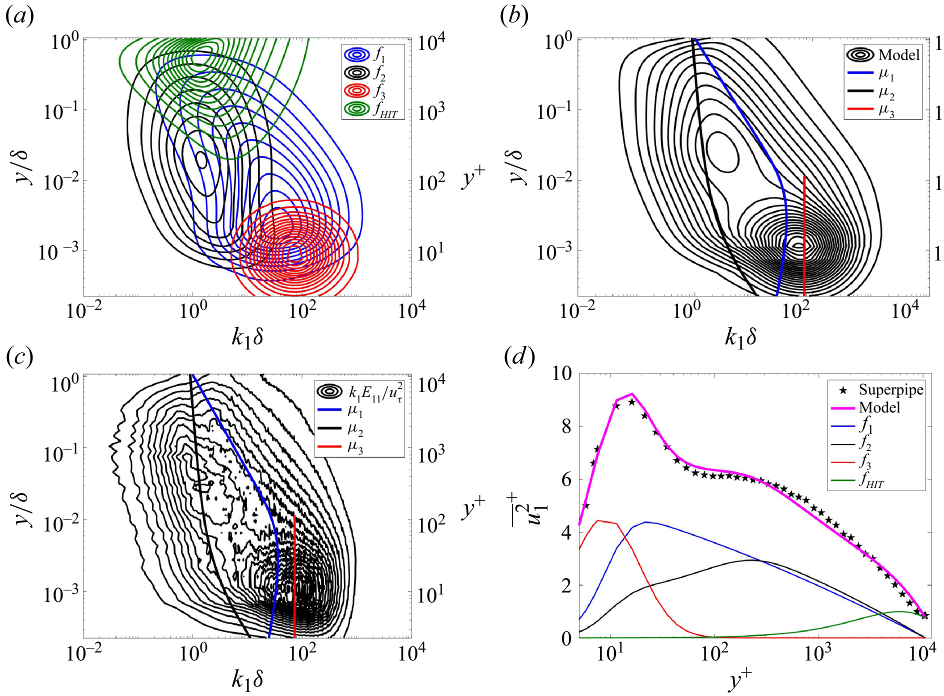

Figure 6. (a,b,c) Contours of $k_1 E_{11}(k_1, y)/u_\tau^2$ at $Re_\tau = 10\,500$: (a) contributions by the four eddy functions f_1, f_2, f_3 and f_{HIT}; (b) model representation (summation of f_1, f_2, f_3 and f_{HIT}); (c) superpipe results (Hultmark *et al.* 2013). Thick blue, black and red lines represent μ_1, μ_2 and μ_3, respectively. Contour spacing is 0.1 for all graphs except for f_{HIT}, where it is 0.02. (d) Comparison of the modelled $\overline{u_1^2}^+$ profile to the data of Hultmark *et al.* (2013), and the individual contributions from f_1, f_2, f_3 and f_{HIT}.

energy contribution from f_2 reduces near the wall. For $y^+ > 100$, the energy content is largely provided by f_1 and f_2, which contribute an equal amount of streamwise energy content, while rolling off logarithmically with increasing y. Within the outer layer, f_{HIT} becomes increasingly important and provides all the streamwise energy content at $y = \delta$ (the pipe centreline).

3.2. *Reynolds number dependence of the stress distributions*

The Reynolds number dependence of the modelled profiles is tested in figure 7 by comparisons with pipe flow data over Reynolds numbers ranging from 180 to 1 00 000. As indicated earlier, the data were drawn from DNS for $180 \leq Re_\tau \leq 6000$ (Pirozzoli *et al.* 2021), the Superpipe experiments for $2000 \leq Re_\tau \leq 1\,00\,000$ (Hultmark *et al.* 2013), and the near-wall PIV CICLoPE profiles for $6000 \leq Re_\tau \leq 40\,000$ (Willert *et al.* 2017).

Despite being formulated in wavenumber space, figure 7(a–c) illustrate how well the integrated model spectra match the energy content relative to the available data over three orders of magnitude in Reynolds number. Some discrepancies are evident, such as a shift towards the wall in the modelled near-wall peak at the lowest Reynolds number that is not seen in the data, but the comparisons illustrate that certain key features of distributions are produced well by the model. Specifically, we refer to the logarithmic scaling in the overlap layer, the formation and growth of a near-wall peak around $y^+ = 15$, and the development of an outer peak in the range $100 < y^+ < 1000$. We now consider these features in more detail.

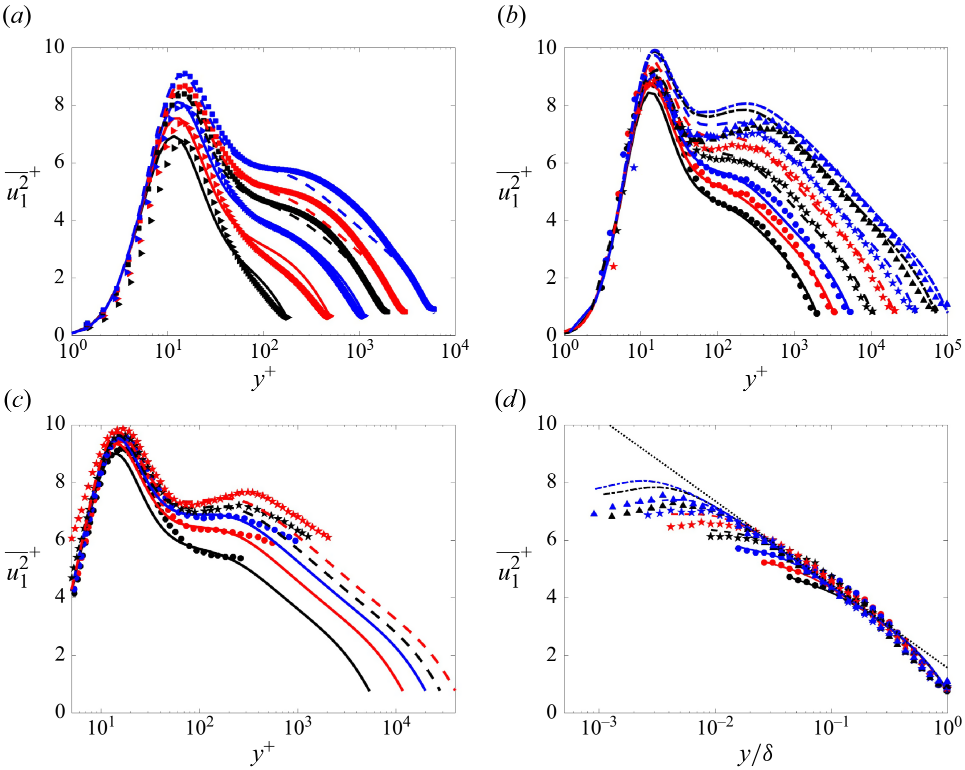

Figure 7. Wall-normal dependence of the $\overline{u_1^2}^+$ values predicted by the model compared in inner scaling to (*a*) pipe flow DNS of Pirozzoli *et al.* (2021), (*b*) NSTAP measurements in the Superpipe of Hultmark *et al.* (2013), and (*c*) PIV measurements in CICLoPE of Willert *et al.* (2017). The Superpipe comparison is also shown in (*d*) using outer scaling and compared to (3.1) for wall-normal locations $y^+ > 100$. In all plots, the lines indicate the model prediction, and the symbols indicate the reference data.

First, consider the logarithmic variation. We expect that at a sufficiently high Reynolds number, in the region where the overlap layer forms in the mean velocity profile, $\overline{u_1^2}^+$ follows a logarithmic variation given by

$$\overline{u_1^2}^+ \approx B - C\ln(y/\delta) \tag{3.1}$$

(Townsend 1976; Perry *et al.* 1986), where $B = 1.56$ and $C = 1.26$ (Hultmark *et al.* 2012, 2013; Marusic *et al.* 2013). Figure 7(*d*) shows how well the model reproduces this logarithmic dependence. Although this result is not unexpected given the formulation of A_1 and A_2, figures 7(*b*) and 7(*d*) also illustrate that the range of wall-normal locations over which this behaviour is apparent is also well reproduced, despite not being explicitly defined within the model. However, figure 7(*a*) does indicate that the logarithmic dependence is over-enforced at low Reynolds number.

Second, consider the Reynolds number dependence of the inner peak at $y^+ \approx 15$. Figure 7 shows that through the superposition of f_1 and f_2 with f_3, the model is able to reproduce the expected behaviour of the inner peak even though it is not explicitly defined in the model. To provide a more quantitative comparison, the Re_τ dependence of the maximum value of the inner peak, $(\overline{u_1^2}^+)_{max}$, is compared to the available DNS and experimental data in figure 8. The model closely follows the fit presented by Lee &

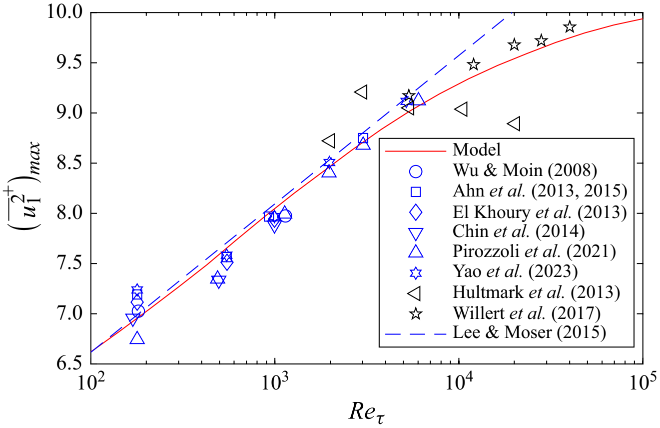

Figure 8. Velocity variance inner peak, $(\overline{u_1^2}^+)_{max}$, for pipe flow as a function of Re_τ. Blue symbols indicate values from DNS; black symbols indicate values from experiments; the red line indicates model prediction; the blue dashed line indicates Lee & Moser (2015) channel flow correlation $(\overline{u_1^2}^+)_{max} \approx 3.66 + 0.642 \ln Re_\tau$.

Moser (2015) up to $Re_\tau \approx 6000$, but then it conforms more closely with the trend observed by Willert *et al.* (2017). Although experiments at higher Reynolds numbers are often affected by spatial filtering (e.g. Hutchins *et al.* 2009; Smits *et al.* 2011*b*; Miller, Estejab & Bailey 2014; Smits 2022), the data from Willert *et al.* (2017) were measured using PIV in a geometrically large facility and have a combined uncertainty of spatial filtering and noise of 1.4 % at $Re_\tau = 11\,600$, 2.7 % at at $Re_\tau = 20\,000$, 4.9 % at $Re_\tau = 28\,000$, and 7.8 % at $Re_\tau = 40\,000$. These uncertainties cannot explain the peak value falling below the extrapolation of Lee & Moser (2015) except at the highest Re_τ values, and even then only if the true value was at the upper limit of the uncertainty bound.

From the perspective of the model, the observation that $(\overline{u_1^2}^+)_{max}$ follows a logarithmic dependence only up to a threshold Reynolds number was found to be caused by a transition away from low Re_τ behaviour in which the outer-scaled attached eddies provide a significant contribution near the wall that increases with Re_τ. As the scale separation increases with Re_τ, the wall damping of the detached f_2 eddies, encapsulated by the inner-scaled α contribution, increasingly shifts the contribution of f_2 to being inner-scaled and thereby minimises the Re_τ dependence of the f_2 contribution to the streamwise energy content at $y^+ = 15$. In other words, the near-wall universal inner-scaled behaviour becomes increasingly important near the wall, as the outer-scaled detached eddies move further from the wall in inner units.

Third, we examine the appearance of an outer peak in $\overline{u_1^2}^+$ at high Re_τ near $y^+ \approx 300$ (e.g. see Fernholz *et al.* 1995; Vallikivi *et al.* 2015; Willert *et al.* 2017; Smits 2022). Vassilicos *et al.* (2015) showed that this peak can occur if there is a range of wavenumbers where the streamwise energy content scales on an intermediate length scale, specifically at wavenumbers corresponding to those of the LSM and VLSM (see also Vallikivi *et al.* 2015). Figure 7(*b*,*c*) indicate that the model predicts the formation of an outer peak, but its peak value $(\overline{u_1^2}^+)_{OP}$ and location $(y^+)_{OP}$ display some discrepancies with experiment. Figure 9(*a*) indicates that although the model predicts a higher peak magnitude than that measured in the Superpipe, it is close to that measured in CICLoPE. Furthermore, the rate at which $(\overline{u_1^2}^+)_{OP}$ increases with Re_τ observed in experiment appears to be closely

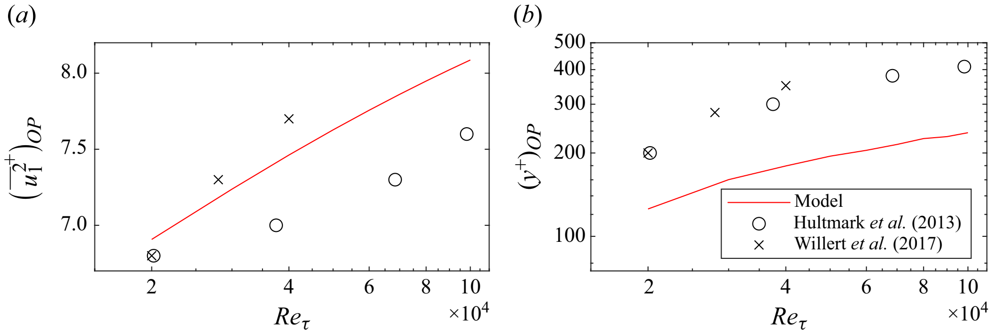

Figure 9. Streamwise Reynolds stress (*a*) outer peak magnitude, and (*b*) location.

reproduced by the model. The Reynolds number dependence in $(y^+)_{OP}$ is also reproduced well by the model, but it predicts the formation of the peak at a lower y^+ location than seen in experiment.

Within the model, the outer peak forms as a consequence of the inner-scaled influence on f_2, represented by α, which produces a maximum in the contribution of f_2 to $\overline{u_1^2}^+$ (as illustrated in figure 6*d*). As Re_τ increases, and the ratio of streamwise energy contained in the outer-scaled eddies increases relative to inner-scaled eddies, the importance of this wall influence on detached eddies results in the emergence of the outer peak. This is consistent with the hypothesis presented by Alfredsson, Segalini & Örlü (2011), who suggested that the outer peak forms as a consequence of scale separation creating a difference in available energy between eddies away from the wall and those near the wall. This is also consistent with the mechanism proposed by Vassilicos *et al.* (2015), although this implies that their intermediate integral scale is not a new scale but rather an indication of the simultaneous presence of inner-scaled and outer-scaled streamwise energy content at the same wall-normal location. Vassilicos *et al.* (2015) also predict that $(\overline{u_1^2}^+)_{OP}$ will increase logarithmically with Re_τ, and that $(y^+)_{OP}$ will increase with Re_τ following a power law. The model prediction does not follow either of these trends, which most likely can be attributed to the bimodal nature of its k_1 dependence.

3.3. *Spectral maps*

Figure 10 provides an overview of the Reynolds number dependence of the energy content in the form of spectral maps of $k_1\,E_{11}(k_1, y)$, where the model predictions are compared to Superpipe data at $Re_\tau = 2000$, 20 400 and 70 000. The experimental results show how at $Re_\tau = 2000$, the spectral map is dominated by an inner spectral peak, corresponding to the peak in streamwise Reynolds stress, and although the spatial filtering increases, as Re_τ increases, the peak moves to increasingly higher $k_1\delta$ values. At higher Re_τ, the increased scale separation both broadens the energy content near the wall, and results in a systematic shift in the spectral energy distribution, appearing as a tilt in the spectral map with respect to the distance from the wall. As previously noted, however, the model is unable to reproduce the details of these spectral maps, but it does capture these effects of scale separation and Re_τ dependence.

Furthermore, the outer peak in the premultiplied spectra of canonical wall-bounded flows, observed when $Re_\tau > 2000$ (e.g. Hutchins & Marusic 2007; Mathis *et al.* 2009*a*; Monty *et al.* 2009), is also apparent in figure 10. Figure 10(*b*,*d*,*f*) demonstrate that the model predicts the emergence of an outer-spectral peak at wall-normal positions and

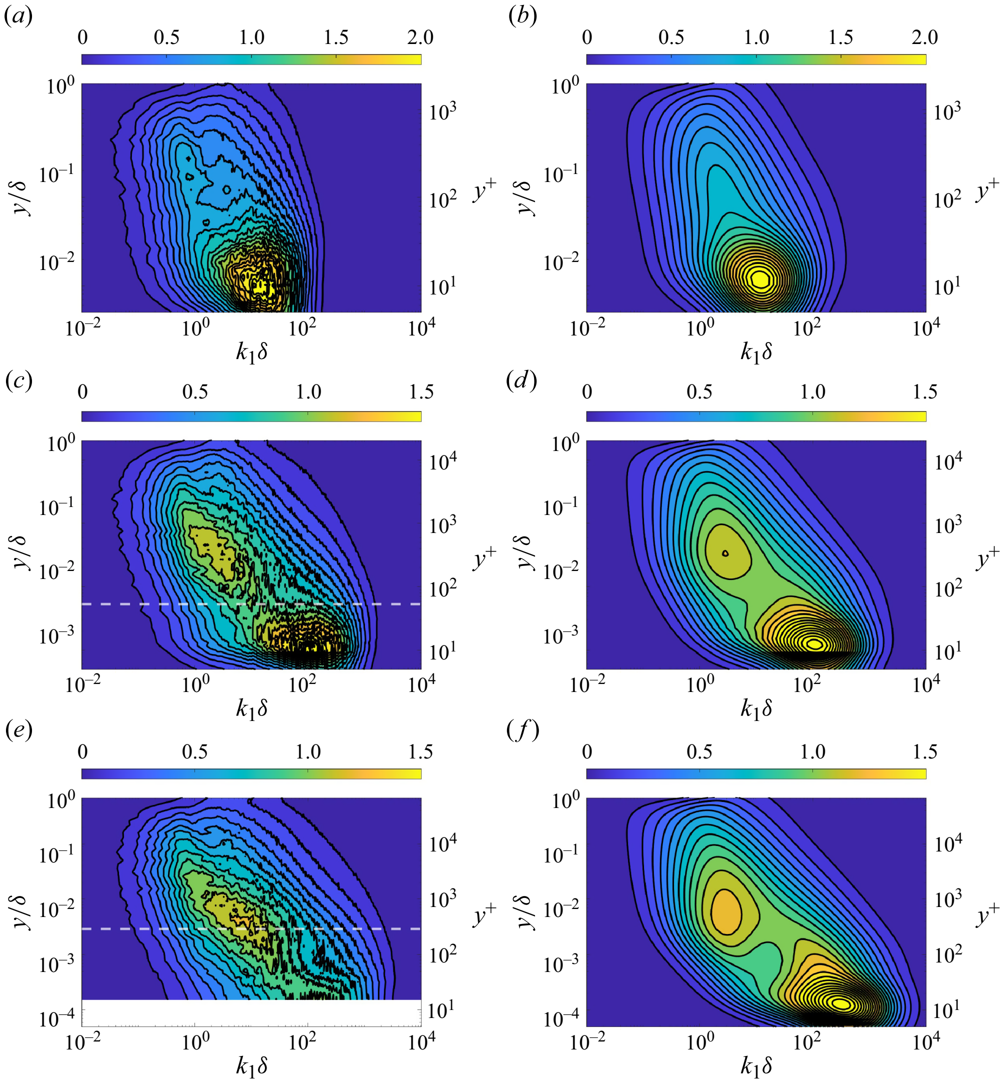

Figure 10. Premultiplied spectral maps of streamwise energy content k_1E_{11}/u_τ^2 for (*a*,*c*,*e*) Superpipe data, (*b*,*d*,*f*) corresponding model prediction, with (*a*,*b*) $Re_\tau = 2000$, (*c*,*d*) $Re_\tau = 20\,400$, (*e*,*f*) $Re_\tau = 70\,000$. White dashed lines in (*c*) and (*e*) indicate wall positions below which spatial filtering corrections according to Hultmark *et al.* (2013) exceed 3 % of the uncorrected value.

wavenumbers similar to those observed in experiment, although a distinct peak becomes apparent only for $Re_\tau > 4000$. As shown in figure 11(*a*), for $Re_\tau < 30\,000$, the model predicts the location of the outer-spectral peak, $(y^+)_{OSP}$, a little closer to the wall than observed in experiments, but with a similar logarithmic trend. Previous studies suggested that $(y^+)_{OSP}$ scales with $Re_\tau^{0.5}$ (Mathis *et al.* 2009*a*; Marusic *et al.* 2013), but the model gives a trend closer to $Re_\tau^{0.4}$. For $Re_\tau > 20\,000$, the data suggest that $(y^+)_{OSP}$ becomes independent of Reynolds number, which is not captured in the model, although spatial filtering may have been important for the experiments at the highest Reynolds numbers (see figure 10*e*). Figure 11(*b*) presents the wavenumber of the outer-spectral peak in inner scaling, $(k_1^+)_{OSP}$, while figure 11(*c*) presents it in outer scaling, $(k_1\delta)_{OSP}$. Although inner

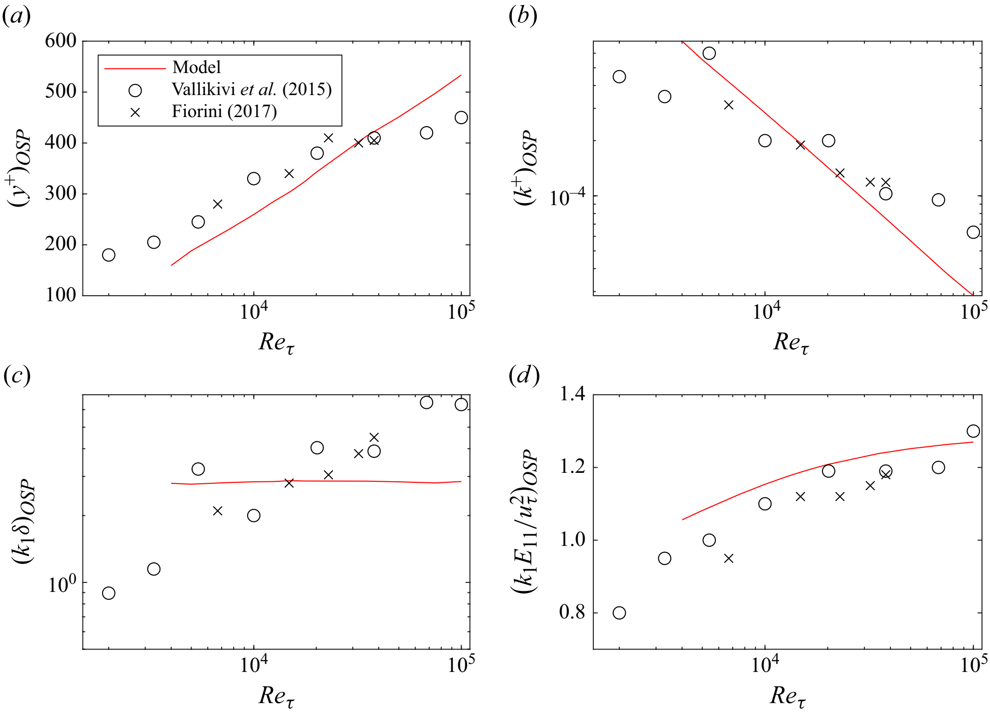

Figure 11. Outer-spectral peak (OSP): (*a*) wall-normal location; (*b*) corresponding wavenumber in inner coordinates; (*c*) wavenumber in outer coordinates; (*d*) peak magnitude. Red line: model prediction. Open circles: Superpipe data (Vallikivi *et al.* 2015). Crosses: CICLoPE data (Fiorini 2017).

scaling captures the general location in wavenumber space over a broad range of Re_τ, the model predicts that $(k_1\delta)_{OSP}$ is independent of Reynolds number, in contrast to the experiments. Nevertheless, the magnitude of the outer-spectral peak $(k_1E_{11}/u_\tau^2)_{OSP}$ is well reproduced by the model, as shown in figure 11(*d*).

In the context of the model, the outer peak arises due to the overlap in wavenumber space of the LSM and VLSM contributions (as illustrated in figure 6(*a*), for example). Whereas the VLSM energy content modelled using f_2 is constrained by inner-scaled wall influence, the LSM energy content is outer-scaled down to $y^+ \approx 20$. As the scale separation increases with Reynolds number, the LSM energy content overlap with the VLSM energy content increases, resulting in the increase in $(y^+)_{OSP}$ with Re_τ. This interpretation suggests that the outer-spectral peak and the outer peak in $\overline{u_1^2}^+$ are related through their source (i.e. contributions from both LSM and VLSM), despite the outer peak in $\overline{u_1^2}^+$ not becoming evident until a much higher Re_τ. With respect to the Reynolds number dependence of $(k_1\delta)_{OSP}$, the inability of the model to capture the data is due to the wavenumber ranges of f_1 and f_2 being defined in outer scaling. This suggests that there are viscous inhibitions on the wavenumber content, at least up to $(y^+)_{OSP}$, that are not captured by the model. Vallikivi *et al.* (2015) also noted that the wavenumber of the outer-spectral peak follows neither inner nor outer scaling, suggesting that, following Vassilicos *et al.* (2015), an alternate integral scale emerges in this region at high Re_τ that is required to scale the attached eddies. However, as observed in our discussion of the outer peak in $\overline{u_1^2}^+$, this intermediate scale is perhaps better described through a co-existence of inner-scaled and outer-scaled eddies in this wavenumber range.

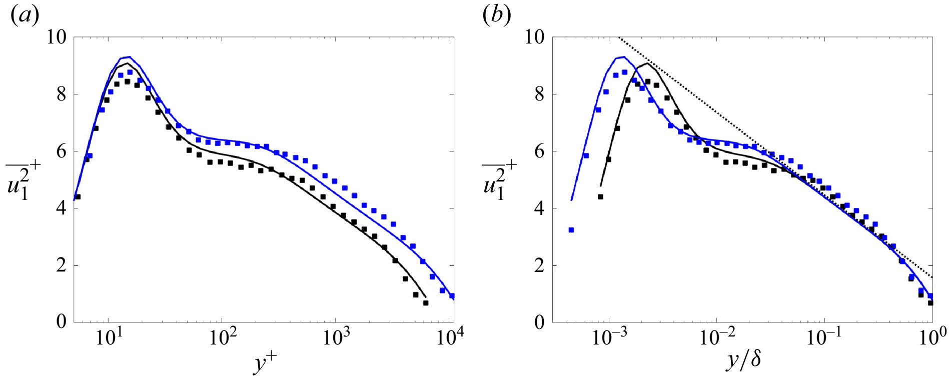

Figure 12. Wall-normal dependence of $\overline{u_1^2}^+$ in boundary layers predicted by the model (lines) to NSTAP measurements in turbulent boundary layers at $Re_\tau = 6500$ (black symbols) and $Re_\tau = 11\,000$ (blue symbols) (Gustenyov *et al.* 2023): (*a*) inner scaling, (*b*) outer scaling.

4. Comparing model results with boundary layer and channel flow data

The characteristic features of boundary layer and channel flows are broadly similar to those seen in pipe flows, and although the model was derived using pipe flow data, it should therefore be possible to adapt the model for these other flows. To illustrate the similarities, the unadapted model results are compared to the turbulent boundary layer data obtained in the High Reynolds Number Boundary Layer Wind Tunnel (HRNBLWT) at the University of Melbourne, Australia, by Gustenyov *et al.* (2023) at $Re_\tau = 6500$ and 11 000 (these data are fully resolved and free of any spatial filtering effects), and to the channel flow DNS of Lee & Moser (2015) at $Re_\tau = 5200$.

For the turbulent boundary layer comparisons, figure 12 demonstrates that the model captures the key features of the $\overline{u_1^2}^+$ profiles but that it under-predicts the streamwise energy content in the logarithmic region by an approximately constant vertical shift (figure 12*b*). This is to be expected, since the additive constant in the log law for the turbulence (3.1) is larger for boundary layers compared to pipe flows: $B = 2.30$ compared to $B = 1.56$ as per Marusic *et al.* (2013). With respect to the spectral distributions of the streamwise energy content, figure 13 shows that the general features are reproduced by the model, but the predicted outer-spectral peak is weaker, and appears closer to the wall than observed in the measured spectral maps. This may be due to the increased importance of the motions attributed to f_1 relative to the motions attributed in f_2 in the boundary layer relative to the pipe, a feature that can be observed when comparing the outer layer of figure 13(*c*) to figure 6(*c*).

For the channel flow comparison at $Re_\tau = 5200$, illustrated in figures 14 and 15, many of the differences observed in the boundary layer/pipe flow comparison are also evident here. There is a tendency for the $\overline{u_1^2}^+$ inner peak to appear at lower y^+ at this Re_τ, and an upward shift in the log-law for the turbulence. To be fair, the model also displays a more extensive log-law dependence that is not observed in the DNS. The spectral maps shown demonstrate a general similarity between the model prediction and the channel DNS, although one notable difference is that the wavenumber at which the outer-spectral peak is evident appears to be lower than observed for the pipe flow cases, and as reflected in the model prediction.

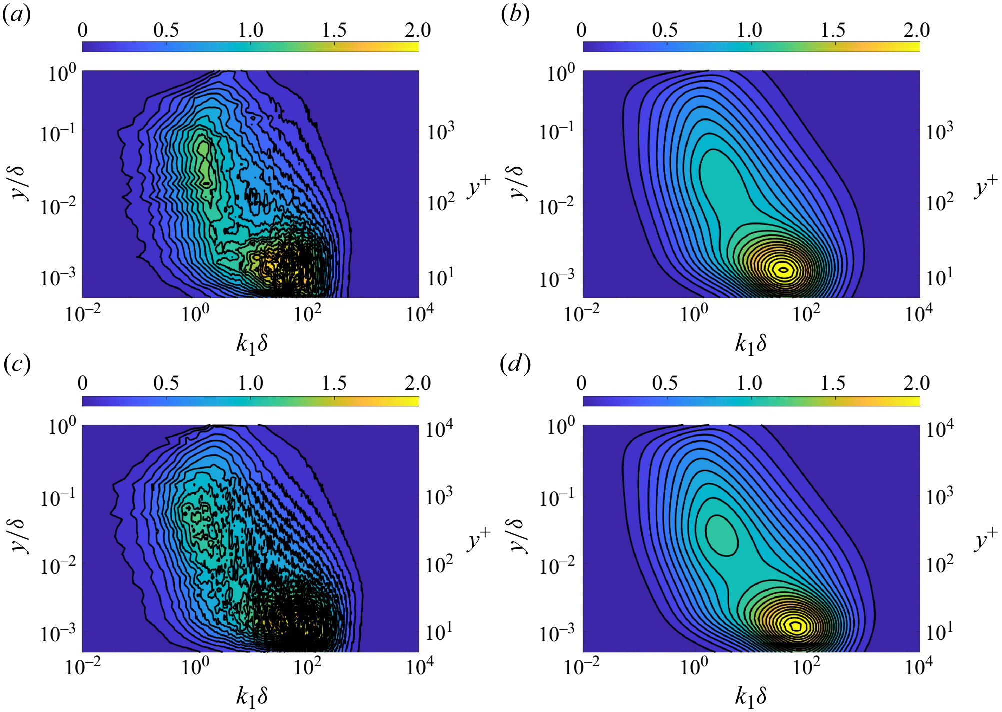

Figure 13. Premultiplied spectral maps of streamwise energy content k_1E_{11}/u_τ^2: (*a*,*c*) NSTAP measurements in turbulent boundary layers, (*b*,*d*) corresponding model prediction, for (*a*,*b*) $Re_\tau = 6500$, (*c*,*d*) $Re_\tau = 11\,400$.

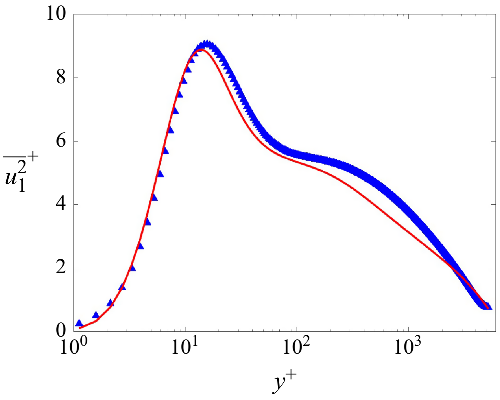

Figure 14. Wall-normal dependence of $\overline{u_1^2}^+$ in channel flow predicted by the model (red line) compared to channel flow DNS (symbols) of Lee & Moser (2015) at $Re_\tau = 5200$.

5. Sensitivity of results to coefficient values

The model requires nine coefficients to be determined (A_n, μ_n and σ_n for each of f_1, f_2 and f_3). The parameters μ_n were derived from features clearly identifiable in the available experimental data, and thereby ensure consistency with those features. In contrast, the parameters A_n and σ_n were determined through a more empirical approach, therefore their values are intrinsically more uncertain. To evaluate the model's sensitivity to these

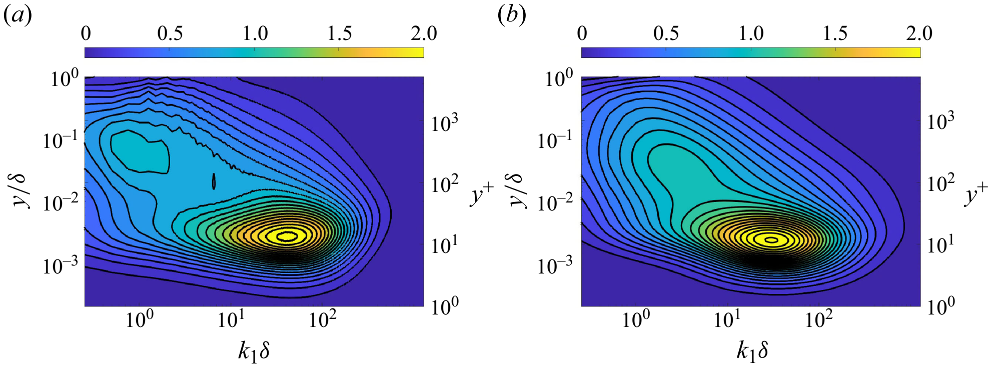

Figure 15. Premultiplied spectral maps of streamwise energy content k_1E_{11}/u_τ^2 at $Re_\tau = 5200$: (*a*) channel flow DNS (Lee & Moser 2015); (*b*) model prediction.

coefficients, each coefficient was independently perturbed by $\pm 10\,\%$. The effects of these perturbations on the streamwise Reynolds stress profile are illustrated in figure 16 for $Re_\tau = 10\,500$. The general shape of each profile remains largely unaffected by these perturbations. Notably, the coefficients exert the greatest influence near the wall, where the Reynolds stresses are highest, which is consistent with the nature of the perturbation being relative rather than absolute in nature. In addition, the results suggest that the model is more sensitive to changes in the amplitude of the eddy populations than to their spread in wavenumber space. As expected, A_3 and σ_3 primarily affect the near-wall peak of the profile. However, A_1 and σ_1 also play significant roles on this feature, underscoring the importance of the superposition of eddy populations in shaping the overall stress distribution. In contrast, the impact of A_2 is mainly confined to the shoulder region of the profile due to the restraining influence of the α parameter reflecting the wall confinement.

Beyond demonstrating the robustness of the model to moderate coefficient variations, these results suggest a potential pathway for adapting the model to other canonical wall-bounded flows. For example, the differences observed in comparing the current pipe-centric version of the model to boundary layers and channel flows, presented in § 4, are within the range of differences shown in figure 16 introduced by adjusting the model coefficients.

6. Conclusions

A model was introduced to predict the one-dimensional streamwise energy spectra and corresponding Reynolds stress profiles for turbulent pipe flow. Constructed using simple log-normal distributions to represent the characteristic eddy populations in wall-bounded flows, the model showcases how such an approach can replicate many key features over three orders of magnitude in Reynolds number, such as the Reynolds number dependence of the inner peak, the formation of a scaling logarithmic region in the overlap layer, and the formation of an outer peak in the streamwise Reynolds stress distribution. The model is also able to reproduce the principal features of the one-dimensional spectrum, even within the near-wall region where three eddy populations exert influence simultaneously. Most notably, the model is able to predict the emergence of an outer-spectral peak, and the Reynolds number dependence of its location and amplitude.

Our model assumes that the contributions from the various eddy populations can be simply summed, and nonlinear interactions can be neglected. Our estimate, based on the analysis of Marusic *et al.* (2010), suggests that the nonlinear modulation interactions have

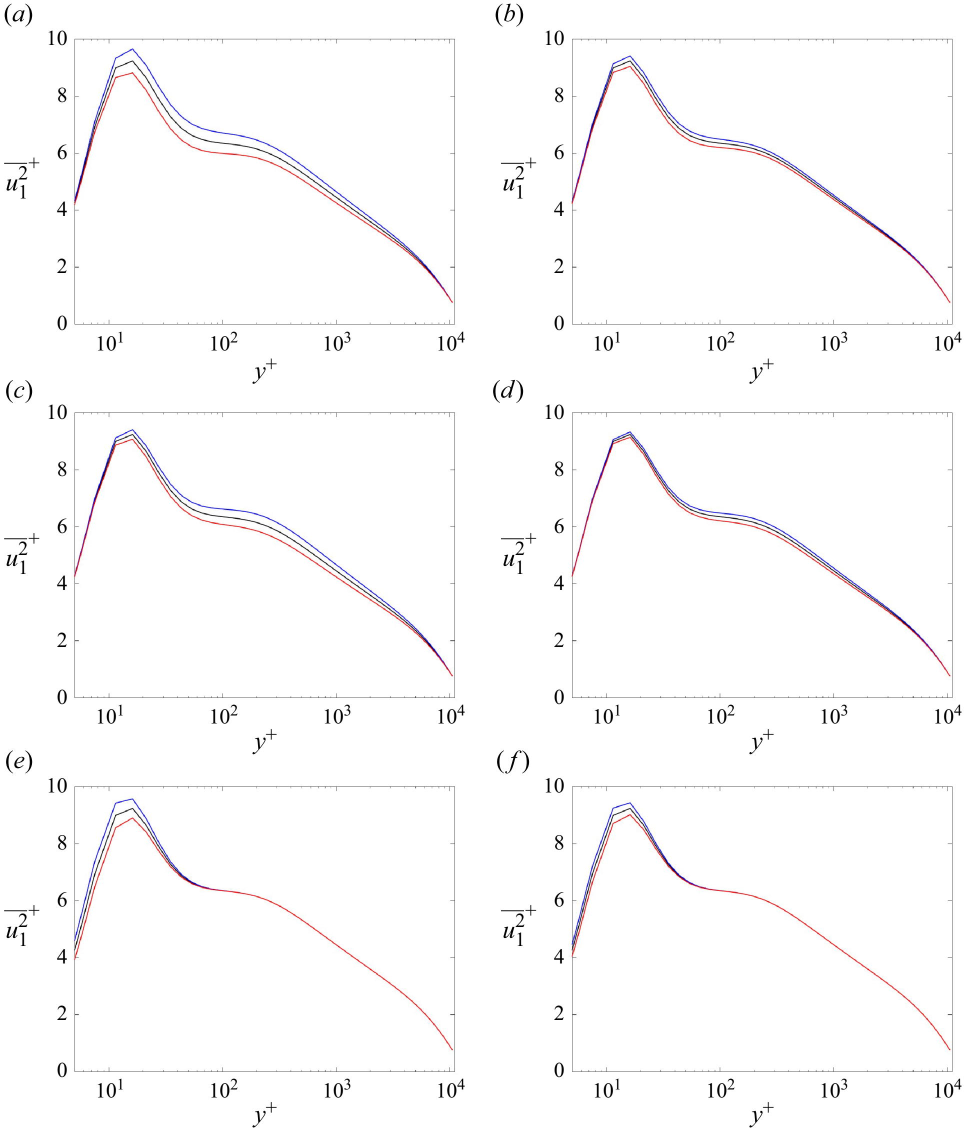

Figure 16. Inner-scaled Reynolds stress, Superpipe at $Re_\tau = 10\,500$. Black lines: original values. Blue lines: +10 %. Red lines: −10 %. Plots for (*a*) A_1, (*b*) σ_1, (*c*) A_2, (*d*) σ_2, (*e*) A_3, (*f*) σ_3.

a negligible influence on the streamwise energy content, and that the superimposition contribution could be introduced via increasing scale separation, combined with the inner-scaled viscous damping of the outer-scaled eddy populations near the wall. The result is overlapping inner- and outer-scaled energy content in wavenumber space, which introduces a Reynolds number dependence in the near-wall features (as also suggested by Marusic *et al.* 2010).

Certain distinctive features, such as the bimodal nature of the spectrum in the outer layer and the Kolmogorov scaling at high wavenumber, remain unreplicated due to limitations inherent in the selection of the log-normal distributions as the basis function. We speculate that additional discrepancies in the streamwise Reynolds stress distribution – such as the tendency of the inner peak to appear too close to the wall at low Reynolds numbers and the outer peak to also occur too close to the wall at high Reynolds numbers – may be rectified through additional modifications of model coefficients, although at the cost of model simplicity.

Although the model coefficients were derived using experimental data from pipe flow, the model also gives reasonable predictions for turbulent boundary layer and channel flows. Certain disparities are observed, but they can be linked to variations in the structural behaviour among these flows. Such structural differences can potentially be recovered through modification of the model parameters. We also anticipate that non-canonical conditions can be incorporated into the model; for example, Harun *et al.* (2013) indicate that the presence of pressure gradients can alter the large coherent structures, which suggests the potential to incorporate these effects by adjusting the corresponding eddy populations accordingly. A framework for roughness can also be similarly introduced by replacing the small-scale eddy population associated with the near-wall streaks with one incorporating the behaviour found in the roughness sublayer. However, these and other extensions of the current version of the model are left to future efforts.

Finally, we add that we would be happy to provide a Matlab script of the model to interested parties upon request.

Funding. A.J.S. was supported by ONR through grant N00014-17-1-2309. N.G. and S.C.C.B. were supported by NASA EPSCoR through award no. 80NSSC19M0144, and by NASA through award no. 80NSSC20M0162.

Declaration of interests. The authors report no conflict of interest.

Appendix A

We have chosen a relatively straightforward way to adapt the model presented herein to accommodate nonlinear interactions using (1.1) following the procedure outlined in Marusic *et al.* (2010). To do so, we note that the small-scale universal eddies u^* are those represented in the model by f_3, therefore it is f_3 that will be amplified by introducing β.

To determine u_{OL}^+, we use the same wall-normal position used to determine β, specifically $y^+ = 3.9\,Re_\tau^{1/2}$. It is then possible to construct f_1 and f_2 at this wall position, and integrate them over wavenumbers $k_1 < 2\pi/\delta$ (to be consistent with the filtering imposed by Marusic *et al.* 2010) and thereby estimate $\overline{{u_{OL}^+}^2}$.

To determine the increase in the variance of the measured signal due to the nonlinear interaction, we take the square of (1.1) and average it, resulting in

$$\overline{{u_p}^2}^+ = \overline{u^{*2}\left[1+\beta u_{OL}^+\right]^2} + 2\alpha\overline{u^*\left[1+\beta u_{OL}^+\right]u_{OL}^+} + \alpha^2\overline{{u_{OL}^+}^2}. \tag{A1}$$

We assume that the near-wall small-scale universal fluctuating velocity signal u^* and the near-wall contribution from the outer-layer motion u_{OL}^+ are zero-mean, uncorrelated and independent, which suggests $\overline{u^* u_{OL}^+} = \overline{u^{*2} u_{OL}^+} = \overline{u^* u_{OL}^{+2}} = 0$ (Bendat & Piersol 2000), which yields (1.2). Furthermore, this implies that $\overline{u^{*2} u_{OL}^{+2}} = \overline{u^{*2}}\;\overline{{u_{OL}^+}^2}$. Thus

$$\overline{{u_p}^2}^+ = \overline{u^{*2}} + \beta^2\,\overline{u^{*2}}\;\overline{{u_{OL}^+}^2} + \alpha^2\,\overline{{u_{OL}^+}^2}. \tag{A2}$$

Note that the superposition described by $\alpha^2\overline{{u_{OL}^+}^2}$ in (1.1) is already captured in the linear superposition of f_1, f_2 with f_3 within the model. Thus the increase in f_3 due to amplitude

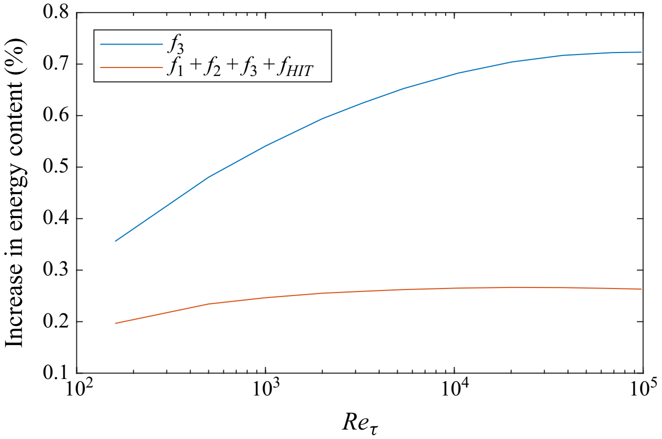

Figure 17. Modulation effect as measured through the percentage increase in the streamwise energy content of f_3 (blue line) and the entire model (red line).

modulation can be represented through

$$f_P = f_3\left(1 + \beta^2\, \overline{u_{OL}^{+\ 2}}\right), \tag{A3}$$

where f_P can now replace f_3 in (2.1).

The impact of this modification on the resulting streamwise energy content is relatively small, as presented in figure 17. This figure presents $\int (f_P/f_3)\, \mathrm{d}k_1 - 1$ and $\int ((f_1 + f_2 + f_P + f_{HIT})/(f_1 + f_2 + f_3 + f_{HIT}))\, \mathrm{d}k_1 - 1$ at $y^+ = 15$. These integrals reflect the percentage increase in the streamwise energy content of just the f_3 contribution, and of the entire $\overline{u_1^2}$ prediction, by the inclusion of the modulation described in (1.1). Using the values for α and β provided by Mathis *et al.* (2011), we can show that the impact of this modulation term is less than 1 % for the range $Re_\tau = 100$ to 1 00 0000.

REFERENCES

ADRIAN, R.J. 2007 Hairpin vortex organization in wall turbulence. *Phys. Fluids* **19** (4), 041301.

AHN, J., LEE, J.H., JANG, S.J. & SUNG, H.J. 2013 Direct numerical simulations of fully developed turbulent pipe flows for $Re_\tau = 180$, 544 and 934. *Intl J. Heat Fluid Flow* **44**, 222–228.

AHN, J., LEE, J.H., LEE, J., KANG, J.-H. & SUNG, H.J. 2015 Direct numerical simulation of a 30R long turbulent pipe flow at $Re_\tau = 3008$. *Phys. Fluids* **27** (6), 065110.

ALFREDSSON, P.H., SEGALINI, A. & ÖRLÜ, R. 2011 A new scaling for the streamwise turbulence intensity in wall-bounded turbulent flows and what it tells us about the 'outer' peak. *Phys. Fluids* **23** (4), 041702.

BAILEY, S.C.C. & WITTE, B.M. 2016 On the universality of local dissipation scales in turbulent channel flow. *J. Fluid Mech.* **786**, 234–252.

BENDAT, J.S. & PIERSOL, A.G. 2000 *Random Data : Analysis and Measurement Procedures*, 3rd edn New York, U.S.A.: Wiley Interscience.

CHIN, C., MONTY, J.P. & OOI, A. 2014 Reynolds number effects in DNS of pipe flow and comparison with channels and boundary layers. *Intl J. Heat Fluid Flow* **45**, 33–40.

EL KHOURY, G.K., SCHLATTER, P., NOORANI, A., FISCHER, P.F., BRETHOUWER, G. & JOHANSSON, A.V. 2013 Direct numerical simulation of turbulent pipe flow at moderately high Reynolds numbers. *Flow Turbul. Combust.* **91** (3), 475–495.

FERNHOLZ, H.H., KRAUSE, E., NOCKEMANN, M. & SCHOBER, M. 1995 Comparative measurements in the canonical boundary layer at $Re\delta_2 \leq 6 \times 10^4$ on the wall of the German–Dutch windtunnel. *Phys. Fluids* **7** (6), 1275–1281.

FIORINI, T. 2017 Turbulent pipe flow – high resolution measurements in CICLoPE. PhD thesis, Università di Bologna, Bologna, Italy.

GUSTENYOV, N., EGERER, M., HULTMARK, M., SMITS, A.J. & BAILEY, S.C.C. 2023 Similarity of length scales in high-Reynolds-number wall-bounded flows. *J. Fluid Mech.* **965**, A17.

HARUN, Z., MONTY, J.P., MATHIS, R. & MARUSIC, I. 2013 Pressure gradient effects on the large-scale structure of turbulent boundary layers. *J. Fluid Mech.* **715**, 477–498.

HULTMARK, M., VALLIKIVI, M., BAILEY, S.C.C. & SMITS, A.J. 2012 Turbulent pipe flow at extreme Reynolds numbers. *Phys. Rev. Lett.* **108** (9), 094501.

HULTMARK, M., VALLIKIVI, M., BAILEY, S.C.C. & SMITS, A.J. 2013 Logarithmic scaling of turbulence in smooth- and rough-wall pipe flow. *J. Fluid Mech.* **728**, 376–395.

HUTCHINS, N. & MARUSIC, I. 2007 Evidence of very long meandering features in the logarithmic region of turbulent boundary layers. *J. Fluid Mech.* **579**, 1–28.

HUTCHINS, N., NICKELS, T.B., MARUSIC, I. & CHONG, M.S. 2009 Hot-wire spatial resolution issues in wall-bounded turbulence. *J. Fluid Mech.* **635**, 103–136.

VON KÁRMÁN, T. 1948 Progress in the statistical theory of turbulence. *Proc. Natl Acad. Sci.* **34** (11), 530–539.

KIM, K.C. & ADRIAN, R.J. 1999 Very large-scale motion in the outer layer. *Phys. Fluids* **11** (2), 417–422.

KLINE, S.J., REYNOLDS, W.C., SCHRAUB, F.A. & RUNSTADLER, P.W. 1967 The structure of turbulent boundary layers. *J. Fluid Mech.* **30** (4), 741–773.

LEE, M. & MOSER, R.D. 2015 Direct numerical simulation of turbulent channel flow up to $Re_\tau \approx 5200$. *J. Fluid Mech.* **774**, 395–415.

MARUSIC, I. & KUNKEL, G.J. 2003 Streamwise turbulence intensity formulation for flat-plate boundary layers. *Phys. Fluids* **15** (8), 2461–2464.

MARUSIC, I., MATHIS, R. & HUTCHINS, N. 2010 Predictive model for wall-bounded turbulent flow. *Science* **329** (5988), 193–196.

MARUSIC, I. & MONTY, J.P. 2019 Attached eddy model of wall turbulence. *Annu. Rev. Fluid Mech.* **51** (1), 49–74.

MARUSIC, I., MONTY, J.P., HULTMARK, M. & SMITS, A.J. 2013 On the logarithmic region in wall turbulence. *J. Fluid Mech.* **716**, R3.

MATHIS, R., HUTCHINS, N. & MARUSIC, I. 2009*a* Large-scale amplitude modulation of the small-scale structures in turbulent boundary layers. *J. Fluid Mech.* **628**, 311–337.

MATHIS, R., HUTCHINS, N. & MARUSIC, I. 2011 A predictive inner–outer model for streamwise turbulence statistics in wall-bounded flows. *J. Fluid Mech.* **681**, 537–566.

MATHIS, R., MONTY, J.P., HUTCHINS, N. & MARUSIC, I. 2009*b* Comparison of large-scale amplitude modulation in turbulent boundary layers, pipes, and channel flows. *Phys. Fluids* **21** (11), 111703.

MILLER, M.A., ESTEJAB, B. & BAILEY, S.C.C. 2014 Evaluation of hot-wire spatial filtering corrections for wall turbulence and correction for end-conduction effects. *Exp. Fluids* **55** (5), 1–13.

MOIN, P. 2009 Revisiting Taylor's hypothesis. *J. Fluid Mech.* **640**, 1–4.

MONTY, J.P., HUTCHINS, N., NG, H.C.H., MARUSIC, I. & CHONG, M.S. 2009 A comparison of turbulent pipe, channel and boundary layer flows. *J. Fluid Mech.* **632**, 431–442.

MONTY, J.P., STEWART, J.A., WILLIAMS, R.C. & CHONG, M.S. 2007 Large-scale features in turbulent pipe and channel flows. *J. Fluid Mech.* **589**, 147–156.

PERRY, A.E. 1982 *Hot-Wire Anemometry*. Oxford University Press.

PERRY, A.E. & ABELL, C.J. 1977 Asymptotic similarity of turbulence structures in smooth- and rough-walled pipes. *J. Fluid Mech.* **79** (4), 785–799.

PERRY, A.E., HENBEST, S. & CHONG, M.S. 1986 A theoretical and experimental study of wall turbulence. *J. Fluid Mech.* **165**, 163–199.

PIROZZOLI, S., ROMERO, J., FATICA, M., VERZICCO, R. & ORLANDI, P. 2021 One-point statistics for turbulent pipe flow up to $Re_\tau \approx 6000$. *J. Fluid Mech.* **926**, A28.

POPE, S.B. 2000 *Turbulent Flows*. Cambridge University Press.

ROSENBERG, B.J., HULTMARK, M., VALLIKIVI, M., BAILEY, S.C.C. & SMITS, A.J. 2013 Turbulence spectra in smooth- and rough-wall pipe flow at extreme Reynolds numbers. *J. Fluid Mech.* **731**, 46–63.

SADDOUGHI, S.G. & VEERAVALLI, S.V. 1994 Local isotropy in turbulent boundary layers at high Reynolds number. *J. Fluid Mech.* **268**, 333–372.

SMITS, A.J. 2010 High Reynolds number wall-bounded turbulence and a proposal for a new eddy-based model. In *Notes on Numerical Fluid Mechanics and Multidisciplinary Design* (ed. M.D.Thiên-Hiêp & P. Sagout), pp. 51–62. Springer.

SMITS, A.J. 2022 Batchelor Prize lecture: measurements in wall-bounded turbulence. *J. Fluid Mech.* **940**, A1.

SMITS, A.J., MCKEON, B.J. & MARUSIC, I. 2011*a* High–Reynolds number wall turbulence. *Annu. Rev. Fluid Mech.* **43** (1), 353–375.

SMITS, A.J., MONTY, J.P., HULTMARK, M., BAILEY, S.C.C., HUTCHINS, N. & MARUSIC, I. 2011*b* Spatial resolution correction for wall-bounded turbulence measurements. *J. Fluid. Mech* **676**, 41–53.

TAYLOR, G.I. 1938 The spectrum of turbulence. *Proc. R. Soc. Lond. A: Math. Phys. Sci.* **164** (919), 476–490.

TOWNSEND, A.A. 1976 *The Structure of Turbulent Shear Flow*. Cambridge University Press.

VALLIKIVI, M., GANAPATHISUBRAMANI, B. & SMITS, A.J. 2015 Spectral scaling in boundary layers and pipes at very high Reynolds numbers. *J. Fluid Mech.* **771**, 303–326.

VALLIKIVI, M. & SMITS, A.J. 2014 Fabrication and characterization of a novel nano-scale thermal anemometry probe. *J. Microelectromech. Syst.* **23** (4), 899–907.

VASSILICOS, J.C., LAVAL, J.-P., FOUCAUT, J.-M. & STANISLAS, M. 2015 The streamwise turbulence intensity in the intermediate layer of turbulent pipe flow. *J. Fluid Mech.* **774**, 324–341.

WILLERT, C.E., SORIA, J., STANISLAS, M., KLINNER, J., AMILI, O., EISFELDER, M., CUVIER, C., BELLANI, G., FIORINI, T. & TALAMELLI, A. 2017 Near-wall statistics of a turbulent pipe flow at shear Reynolds numbers up to 40 000. *J. Fluid Mech.* **826**, R5.

WU, X. & MOIN, P. 2008 A direct numerical simulation study on the mean velocity characteristics in turbulent pipe flow. *J. Fluid Mech.* **608**, 81–112.

YAO, J., REZAEIRAVESH, S., SCHLATTER, P. & HUSSAIN, F. 2023 Direct numerical simulations of turbulent pipe flow up to $Re_\tau \approx 5200$. *J. Fluid Mech.* **956**, A18.